

# **Rational Design and Mechanical Understanding of Three-Dimensional Macro-/Mesoporous Silicon Lithium-Ion Battery Anodes with Tunable Pore size and Wall Thickness**

Xiuxia Zuo<sup>†a</sup>, Yi Wen<sup>†\*b</sup>, Yike Qiu<sup>†c</sup>, Ya-Jun Cheng<sup>\*a, d</sup>, Shanshan Yin<sup>a, e</sup>, Qing Ji<sup>a, f</sup>, Zhong You<sup>g</sup>, Jin Zhu<sup>a</sup>, Peter Müller-Buschbaum<sup>e, h</sup>, Lifeng Ma<sup>\*c</sup>, Peter G Bruce<sup>d, i, j</sup>, and Yonggao Xia<sup>\*a, k</sup>

- <sup>a</sup>. Ningbo Institute of Materials Technology & Engineering, Chinese Academy of Sciences, 1219 Zhongguan West Rd, Ningbo, 315201, Zhejiang Province, P. R. China
- <sup>b</sup>. National Demonstration Center for Experimental Mechanics Education, School of Aerospace, Xi'an Jiaotong University, 28 Xianning West Rd, Xi'an 710049, Shaanxi Province, P. R. China
- <sup>c</sup>. Department of Engineering Mechanics, Xi'an Jiaotong University, 28 Xianning West Rd, Xi'an 710049, Shaanxi Province, P. R. China
- <sup>d</sup>. Department of Materials, University of Oxford, Parks Rd, OX1 3PH, Oxford, UK
- <sup>e</sup>. Physik-Department, Lehrstuhl für Funktionelle Materialien, Technische Universität München, James-Frank-Strasse 1, 85748 Garching, Germany
- <sup>f</sup>. The University of Nottingham Ningbo China, 199 Taikang East Road, Ningbo, 315100, Zhejiang Province, P. R. China
- <sup>g</sup>. Department of Engineering Science, Parks Road, University of Oxford, Oxford, OX1 3PJ, U.K.
- <sup>h</sup>. Heinz Maier-Leibnitz Zentrum (MLZ), Technische Universität München, Lichtenbergstr. 1, 85748 Garching, Germany
- <sup>i</sup>. The Henry Royce Institute, Parks Road, Oxford, OX1 3PH, UK
- <sup>j</sup>. The Faraday Institution, Quad One, Becquerel Avenue, Harwell Campus, Didcot, OX11 0RA, UK
- <sup>k</sup>. Center of Materials Science and Optoelectronics Engineering, University of Chinese Academy of Sciences, 19A Yuquan Rd, Shijingshan District, Beijing 100049, P. R. China

\*Corresponding author.

Email address: wenyi@mail.xjtu.edu.cn, chengyj@nimte.ac.cn, xiayg@nimte.ac.cn, malf@mail.xjtu.edu.cn

<sup>†</sup>X.Z., Y.Wen., and Y.Q. contribute equally to this work.

## **ABSTRACT:**

Silicon is regarded as one of the most promising next generation lithium-ion battery anodes due to its exceptional theoretical capacity, appropriate voltage profile and vast abundance. Nevertheless, huge volume expansion and drastic stress generated upon lithiation cause poor cyclic stability. It has been one of the central issues to improve cyclic performance of silicon based lithium-ion battery anodes. Constructing hierarchical macro-/mesoporous silicon with tunable pore size and wall thickness is developed to tackle this issue. Rational structure design, controllable synthesis and theoretical mechanical simulation are combined together to reveal fundamental mechanisms responsible for an improved cyclic performance. A self-templating strategy is applied using Stöber silica particles as templating agent and precursor, coupled with a magnesiothermic reduction process. Systematic variation of the magnesiothermic reduction time allows a good control over the structures of the porous silicon. Finite element mechanical simulations on the porous silicon show that an increased pore size and a reduced wall thickness generate less mechanical stress in average along with an extended lithiation state. Besides the mechanical stress, the evolution of strain and displacement of the porous silicon is also elaborated with the finite element simulation.

**KEYWORDS:** Lithium-Ion Battery Anode; Porous Silicon; Magnesiothermic Reduction; Finite Element Mechanical Simulation

## INTRODUCTION

Silicon (Si) has been recognized as a promising candidate for next-generation lithium-ion battery anodes due to its very high theoretical capacity (*ca.* 4200 mAh g<sup>-1</sup>), reasonable safety associated with an appropriate delithiation potential (around 0.5V vs. Li/Li<sup>+</sup>), environmental friendliness and huge abundance<sup>1-7</sup>. However, poor cyclic stability caused by drastic volume expansion upon lithiation has significantly hampered its practical applications so far. It has been realized that porous silicon can improve the cyclic performance because the pores effectively accommodate volume expansion and mitigate stress concentration as well<sup>8-13</sup>. Consequently, the structural integrity of the individual silicon, the overall stability of the electrode, the connection between electrode and current collector, and the stability of the solid electrolyte interface layer (SEI) can be significantly enhanced<sup>14-16</sup>.

Studies have been reported to synthesize porous silicon with various methods such as wet etching<sup>17-19</sup>, chemical de-alloying<sup>20-23</sup>, templating synthesis<sup>24</sup>, and magnesiothermic reduction<sup>25-27</sup>. Nevertheless, the use of toxic or expensive materials and/or the sophisticated and time-consuming assembly process makes the former three methods difficult to scale up. Magnesiothermic reduction has been demonstrated to be a facile method for the bulk synthesis of porous silicon with varying degrees of structural control<sup>28-32</sup>.

Integration of both macro and meso-sized porous structures is an effective way to accommodate volume change and alleviate mechanical stress of the silicon anode. Macropores can accommodate the huge volume change; while mesopores are capable of providing sufficient surface area for electrolyte wetting, charge carrier transport, and enhanced electrochemical kinetics. However, the number of the studies on hierarchical macro-/mesoporous silicon anodes is still rather limited<sup>33-37</sup>. Particularly, fundamental studies on rational design, controllable synthesis, and mechanical response of the macro-/mesoporous silicon anodes are yet to be developed.

Recently, a new strategy was developed by our group to construct three dimensional hierarchical macro-/mesoporous silicon based on a self-templating mechanism through magnesiothermic reduction. Stöber silica particles were used as templating agents and precursor for silicon simultaneously<sup>38-39</sup>. Because of the synergistic contribution from both the macro and mesopores, the electrochemical performance of the hierarchical porous silicon was significantly improved, which is much better than those of the commercial nanometer and micrometer sized silicon<sup>38</sup>.

Finite element simulation has been employed to understand the mechanical response in the silicon anode upon lithiation<sup>40-42</sup>. Typically, the mechanical perspective of the silicon lithiation is contributed by the elastic, plastic, and electrochemical parts. Considering a softening phenomenon is observed with extended lithiation, it is of importance to describe the mechanical response along with increasing lithiation. So far, major simulation work is focused on individual silicon particles, silicon film, and silicon wire<sup>43-46</sup>. To our best knowledge, very few simulation work has been reported about the macroporous silicon<sup>47</sup>. In the present work, fundamental investigations are carried out with both experimental and computational approaches. The mechanisms for morphology control, mechanical response to lithiation and improved electrochemical performance of the hierarchical macro-/mesoporous silicon anodes are explored. It is found that the pore size, wall thickness, and porosity of the macro-/mesoporous silicon can be tuned by simply varying the reduction time and post-treatment method. Finite element simulation reveals that the detailed structure features of the porous silicon play crucial roles in the mechanical response to lithiation, which confirms the structure origin responsible for the improved electrochemical performance.

## EXPERIMENTAL DETAILS

**Chemicals:** Tetraethyl orthosilicate (TEOS,  $\geq 96\%$ ), ammonium hydroxide ( $\text{NH}_3 \cdot \text{H}_2\text{O}$ , 25 % - 28 %), ethanol ( $\text{EtOH}$ ,  $\geq 99.5\%$ ), magnesium (Mg, 100 mesh - 200 mesh,  $\geq 99\%$ ), hydrochloric

acid (HCl, 36.0 % - 38.0 %) and hydrofluoric acid (HF,  $\geq 40$  %) were bought from Sinopharm Group Co., Ltd. Sodium alginate was purchased from Aladdin. Conductive carbon black (Super P,  $\geq 99$  %) was obtained from Alfa Aesar. Nano-sized silicon (30 nm,  $> 99.9$  %) was obtained from HaoTian Nano Technology (Shanghai) Co., Ltd. Micro-sized silicon (2  $\mu\text{m}$  - 10  $\mu\text{m}$ ,  $> 99.9$  %) was donated by Fuzhou Sunout Energy & Material Technology Inc. All chemicals were used as received without further purification.

**Sample Preparation:** Monodisperse silica ( $\text{SiO}_2$ ) solid spheres with a diameter of  $410 \pm 8$  nm were prepared according to our previous work.<sup>38</sup> Then the as-synthesized  $\text{SiO}_2$  spheres and magnesium powder were well mixed with a mass ratio of 1:1 and introduced into a corundum boat, which was heated in a tube furnace at 700 °C under Ar /H<sub>2</sub> (volume ratio: 95/5) atmosphere with a ramp rate of 5 °C min<sup>-1</sup>. To tune the morphology of the porous silicon, the magnesiothermic reduction time was varied as 4 hours, 8 hours, and 16 hours. The obtained crude product was firstly stirred in 1 M HCl solution for 6 hours to remove MgO and then immersed in 4% HF for 1 hour to remove unreacted  $\text{SiO}_2$ . The samples treated with HCl were named as HCl-4h, HCl-8h, and HCl-16h respectively, which were grouped as the HCl-washing samples. Alternatively, the HF etching sample group referred to the HCl washing samples further treated with HF, which were indexed as HF-4h, HF-8h, and HF-16h respectively.

**Material Characterization:** X-ray powder diffraction (XRD) was carried out with  $2\theta$  ranging between 5 ° and 90 ° by a Bruker AXS D8 Advanced X-ray diffractometer with Cu K $\alpha$  radiation ( $\lambda = 0.15406$  nm). Scanning electron microscopy (SEM) was performed by a Hitachi S4800 field-emission scanning electron microscope at an accelerating voltage of 4.0 kV. Transmission electron microscopy (TEM) and high-resolution transmission electron microscopy (HRTEM) images were collected on JEOL transmission electron microscope operated at 200 kV. Nitrogen adsorption/desorption isotherms were obtained using Micromeritics ASAP2020 Accelerated Surface Area and Porosimetry System. Specific surface areas and pore size distributions were calculated with the Barrett-Joyner-Halenda (BJH) method based on the

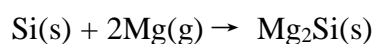
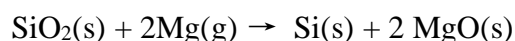
Brunauer-Emmett-Teller (BET) theory. The tap density was measured by vibrating the 1.0 mL graduated cylinder containing the sample of around 0.20 g up and down for 3000 times.

**Electrochemical Measurement:** The electrochemical properties were tested with CR 2032 coin-type cells using either the “HCl-washing” silicon or the “HF-etching” silicon as the active material and lithium metal as the counter electrode. The working electrode was fabricated by casting aqueous slurry on copper current collector with a doctor blading method. The slurry was composed of the as-synthesized Si, sodium alginate and Super P with a mass ratio of 7:2:1. After casting, the electrode was dried at 40 °C for 8 hours. The typical mass loading density of the electrode was controlled to be more than 1.0 mg cm<sup>-2</sup> regarding the mass of the silicon. Cell assembly was carried out in an argon-filled glove box with both moisture and oxygen contents below 0.1 ppm. Commercial electrolyte containing 1.0 M of lithium hexafluoro phosphate (LiPF<sub>6</sub>) in a mixture of ethylene carbonate (EC) and dimethylene carbonate (DMC) (volume ratio 1:1) was used (Zhangjiagang Guotai-Huarong Chemical New Material Co., Ltd.). The cells were aged for 24 hours before electrochemical test.

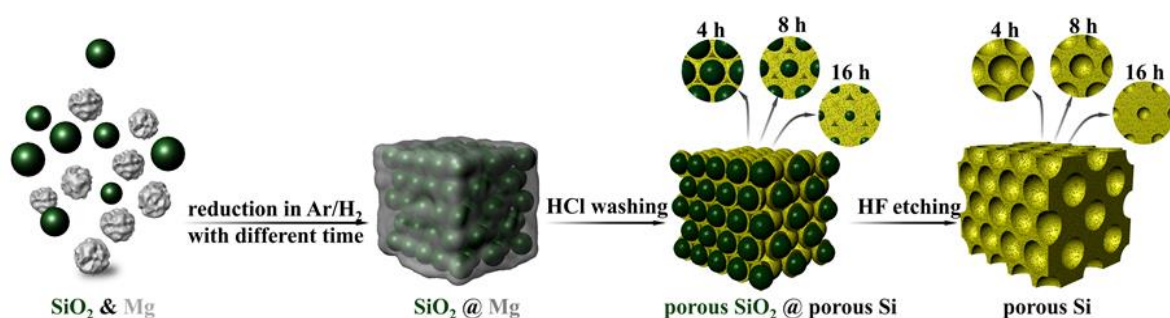
The rate capability and cyclic performance were tested on a multichannel Land Battery Test System. The rate performance was measured at the current density sequence of 0.1 C, 0.2 C, 0.5 C, 1.0 C, 2.0 C, 5.0 C and 0.1 C in a voltage range between 3.0 V and 0.005 V (vs. Li/Li<sup>+</sup>) (five cycles each current density, 1 C = 1000 mAh g<sup>-1</sup>). The cyclic measurement was carried out at a current density of 0.2 C in the voltage range of 3.0 V - 0.005 V (vs. Li/Li<sup>+</sup>) for 100 rounds. The specific capacity was calculated based on the mass of only the active material. The cyclic voltammetry (CV) scans and electrochemical impedance spectroscopy (EIS) data were collected on a Solartron Analytical. For the CV test, a voltage range from 0.001 V to 3.0 V and a scanning rate of 0.2 mVsec<sup>-1</sup> were applied. The EIS measurement was carried out with the frequency range between 0.001 Hz and 1 MHz and amplitude of 10 mV.

## RESULTS AND DISCUSSION

The synthesis process of the 3D macro-/mesoporous silicon is schematically summarized in **Scheme 1**. SiO<sub>2</sub> and Mg powder were firstly mixed together to get a homogeneous powder mixture and then heated to 700 °C under Ar/H<sub>2</sub> flow. The Mg metal is melted at 700 °C and the silica particles forms colloidal packing within the Mg melt, where the magnesiothermic reduction process proceeds from outside to inside of the SiO<sub>2</sub> particles<sup>38</sup>. The SiO<sub>2</sub> precursors are converted to Si/MgO/SiO<sub>2</sub>/Mg<sub>2</sub>Si composite, which is further treated by HCl and HF acid to get the HCl-washing samples and HF-etching samples. The reactions occurred as below<sup>48</sup>:



Based on the self-templating mechanism proposed in our previous work<sup>38</sup>, the effects of reduction time and post-treatment on the structure of the 3D macro-/mesoporous silicon are elaborated in **Scheme 1**. The conversion from silica to silicon is increased as the reduction time extends. As a result, more *in situ* formed silicon is fused together to build up a thickened continuous network, leaving less quantities of un-reacted silica residing in the holes of the silicon network. Thus, extended reduction time and HF-treatment generate 3D macro-/mesoporous silicon with smaller pores and thicker walls. Conversely, a short reduction time leads to a low conversion of silica to silicon. 3D macro-/mesoporous silicon with larger pores and thinner walls is therefore produced after HF treatment. The structural evolution under different reduction time revealed by both SEM and TEM verifies that silica particles act as a self-template to induce the formation of 3D interconnected macroporous structure. The size of the macropores and wall thickness of the three dimensional network can be systematically tuned by varying the magnesiothermic reduction time.



**Scheme 1.** Schematic figure of the self-templating construction and morphology tuning of the 3D hierarchical macro-/mesoporous silicon

The structures of the samples obtained after different reduction time and post treatments are characterized by SEM (**Figure 1**). Figure 1a, 1d, and 1g indicate that the extended reaction time does not modify the size and shape of the HCl-washing samples, which reflect the morphology of the original SiO<sub>2</sub> precursor (Figure S1). The surface of the HCl-washing particles becomes rough compared to the smooth surface of the pristine SiO<sub>2</sub> particles because of the reaction between the silica and magnesium liquid/gas. After further treated with HF, a distinct morphology change is discovered (Figure 1b, 1e, and 1h). Three dimensional (3D) macroporous bulk structures are presented in the HF-4h, HF-8h and HF-16h samples. The macropores resemble the shape of the spherical particles observed in the HCl-washing samples, which suggests that the HF treatment removes the un-reacted silica particles to form 3D continuous macroporous silicon network. The low magnification SEM images in Figure S2 confirm that the spherical particles of the HCl-washing samples and macroporous structures of the HF-etching samples are all uniform in regions with a length scale of around 10  $\mu\text{m}$ . High magnification SEM images (Figure 1c, 1f, and 1i) indicate that small differences exist among the HF-etching samples. The average diameters of the pores for the HF-4h, HF-8h and HF-16h samples are  $381\pm10$  nm,  $352\pm11$  nm and  $339\pm11$  nm, respectively (averaging based on ten data points). The pore diameters decrease with extended reduction time. Correspondingly, the pore walls of the HF-4h, HF-8h, and HF-16h are gradually thickened with elongated reaction time, which are measured to be  $37\pm6$  nm,  $69\pm12$  nm and  $87\pm9$  nm, respectively. The increased reduction time promotes the magnesiothermic reduction of the silica particles. As a result, more silica is converted to silicon, which reduces the diameter of the unreacted silica and increases the wall thickness simultaneously. It is worth noticing that the sum of the pore diameter and wall thickness generally remains constant with respect to the three HF-etching samples, which is close to the diameter of the pristine silica particles. It confirms that the silica particles act as templating agents to guide formation of the macroporous silicon.



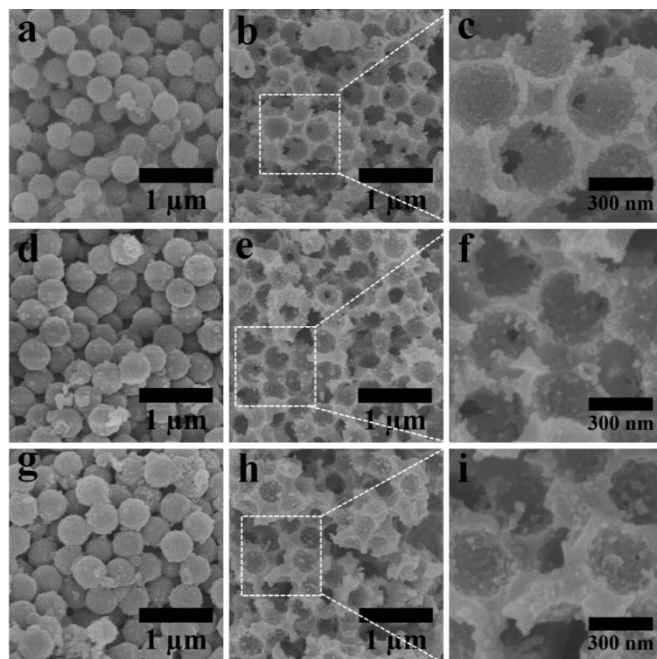


**Figure 1.** SEM images of porous silicon samples. (a) HCl-4h, (b, c) HF-4h, (d) HCl-8h, (e, f) HF-8h, (g) HCl-16h, and (h, i) HF-16h.

The TEM images further uncover the structure details of the macroporous silicon obtained with different reduction time and post treatments (**Figure 2**). Figure 2a, 2c and 2e unveil that the HCl washing samples bear spherical structures with almost the same diameters of about 400 nm. Particularly, the spheres are not solid in nature as compared to pristine SiO<sub>2</sub> (Figure S1). Instead, porous structures are observed because of the etching process induced by the magnesium liquid/gas. Furthermore, the TEM images show that the spheres are inter-connected with each other, which is difficult to be visualized by SEM in Figure 1a, 1d, and 1g. The inter-connected network is not fully solid and mesopores can be observed in the TEM images. Further HF treatment of the HCl washing samples removes the unreacted silica spheres, which gives rise to macropores as shown by the TEM images of Figure 2b, 2d, and 2f. The average sizes of the macropores are also determined based on the TEM images. The diameters gradually decrease from  $382 \pm 8$  nm to  $351 \pm 15$  nm and  $332 \pm 12$  nm with increasing reduction time from 4 hours to 8 hours and 16 hours. The results obtained from the TEM images are generally consistent with the SEM images. Nevertheless, it is difficult to measure the wall thickness of the macroporous silicon precisely because the wall regions in the TEM images are smeared and no clear boundary can be defined. Both the SEM and TEM imaging

results indicate that the increased reduction time converts more silica to silicon, thereby leading to a reduced pore size and an enlarged wall thickness. The enhanced reduction extent is also confirmed by a systematic mass increase retained after HF etching. It is found that around 33 %, 40 %, and 55 % of the mass is retained after HF etching regarding the reduction time of 4 hours, 8 hours, and 16 hours. Therefore, the conversion yield from SiO<sub>2</sub> to Si by the magnesium reduction is calculated to be 51 %, 58 %, and 72 %, respectively. The macropores are still inter-connected with each other after HF etching by the *in situ* formed silicon as shown by both SEM and TEM. Mesopores are present within the continuous silicon network after HF treatment as shown by the TEM images in Figure 2b, 2d, and 2f. Therefore, it is reasonable to conclude that hierarchical macro-/mesoporous silicon is successfully synthesized through the magnesiothermic reduction for a time ranging from 4 hours to 16 hours at 700 °C followed by HF etching.

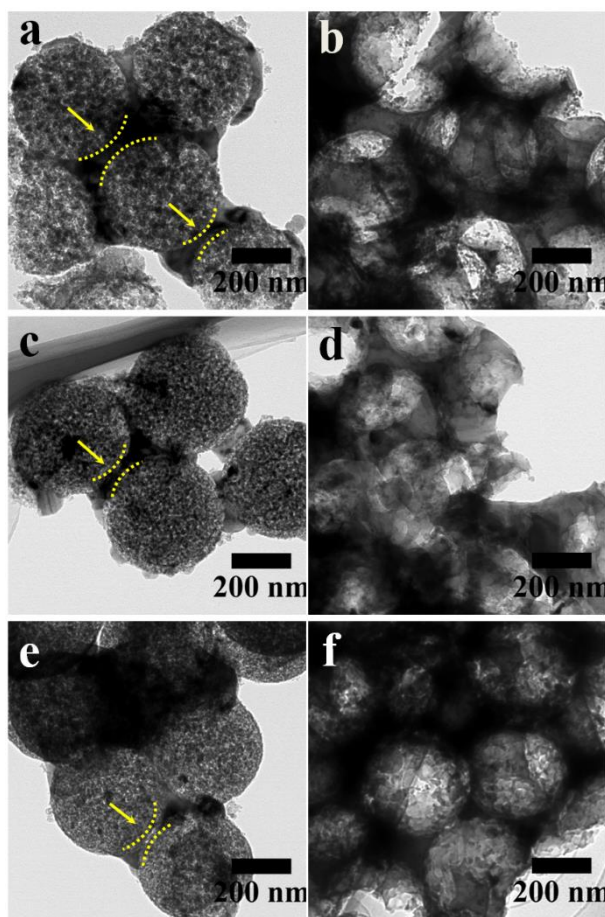


**Figure 2.** TEM images of porous silicon samples. (a)HCl-4h, (b)HF-4h, (c)HCl-8h, (d)HF-8h, (e)HCl-16h, and (f)HF-16h. (The arrows pointed out the interconnected part between the adjacent spheres).

The detailed structure information such as crystallographic phase and porosity of the porous silicon is characterized by XRD, HRTEM, and nitrogen adsorption/desorption measurement, respectively. As shown by the XRD profiles in Figure S3, the amorphous silica is converted to crystalline silicon after the magnesiothermic reduction for 4 hours, 8 hours, and 16 hours. Particularly, a broad diffraction peak belonging to the amorphous silica is observed for the HCl-4h sample (Figure S3b), which is not visible in the samples with the reduction time of 8 h and 16 h (Figure S3c and S3d). It indicates that the extended reaction time converts more silica into silicon. After further HF treatment, the broad peak disappears, which suggests that the residual amorphous silica is totally removed (Figure S3b). It further confirms that the residual silica within the HCl washing samples can be completely etched away by HF. Besides XRD, the HRTEM images combined with the SAED patterns shown in Figure S4 also confirm that crystalline silicon is acquired in both HCl-washing and HF-etching samples after magnesiothermic reduction for different time ranges.

Porosity information including pore size distribution, specific surface area and pore volume of the HCl-washing samples and HF-etching silicon is shown in Table 1 and Figure S5. The BET surface areas and pore volumes of the HCl-washing samples increase gradually along with increasing reduction time because the formation of mesopores is enhanced during the magnesium thermal reduction of the silica particles. After HF etching, the specific surface areas of the samples for the reduction time of 8 h and 16 h are decreased because mesoporous silica particles are removed. Nevertheless, the 4 h sample exhibits a reverse trend, where the specific surface area is slightly increased after HF etching. A limited amount of mesoporous structure is created in the silica particles with a reduction time of 4 h. As a result, the removal of the mesoporous silica particles does not reduce the total surface area significantly. Instead, the actual mass of the sample is reduced due to removal of the silica particles, leading to an increased overall specific surface area. The BET specific surface areas of the HF-etched samples are continuously increased with extended reaction time. Nevertheless, the pore volume is gradually decreased with the reaction time. The increased pore volume from the mesopores cannot balance the diminished pore volume due to decreased

diameters of the macropores, leading to a reduced total pore volume. Detailed analysis about the porosity of the porous silicon is elaborated in the supporting information.

**Table 1.** Summary of the porosity information of the HCl-washing and HF-etching samples

Samples	BET surface area (A) ( $\text{m}^2\text{g}^{-1}$ )	Pore volume (V) ( $\text{cm}^3\text{g}^{-1}$ )	Pore diameter (nm)	Macropores diameter (nm)	Wall thickness (nm)
HCl-4h	79.2	0.26	13.1	/	/
HCl-8h	215.1	0.56	10.4	/	/
HCl-16h	257.5	0.64	9.9	/	/
HF-4h	110.3	0.57	20.6	381 $\pm$ 10	37 $\pm$ 6
HF-8h	118.6	0.45	15.1	352 $\pm$ 11	69 $\pm$ 12
HF-16h	134.3	0.41	12.2	339 $\pm$ 11	87 $\pm$ 9

The electrochemical properties of the porous silicon electrodes as lithium-ion battery anodes are investigated. Figure S6 shows the CV curves of the HCl-washing and HF-etching samples. All electrodes exhibit similar CV behaviors, showing lithiation and delithiation peaks at typical potentials for the reaction of  $\text{Si}^{49}$ . Figure S7 gives the discharge/charge profiles of the porous silicon electrodes, which are similar to the behavior of the nano-sized  $\text{Si}^{38}$ . The voltage plateaus agree well with the lithiation and delithiation peaks displayed in the CV curves. The initial discharge/charge capacities and initial columbic efficiencies (ICE) of the porous silicon are summarized in **Table 2 and Table 3**. Regarding the HCl-4h, HCl-8h and HCl-16h samples, the discharge capacities are 499  $\text{mAhg}^{-1}$ , 975  $\text{mAhg}^{-1}$  and 1562  $\text{mAhg}^{-1}$  against the total mass of the active material, respectively. Considering that the silicon content is 33 %, 40 % and 55 % for the reduction time of 4 h, 8 h, and 16 h, the increase in the discharge capacities is beyond the values normalized to the actual contents of silicon. Specifically, while the HCl-4h sample only exhibits the capacity of 1512  $\text{mAh g}^{-1}$  against the silicon content, the HCl-8h and HCl-16h exhibit capacities of 2438  $\text{mAh g}^{-1}$  and 2840  $\text{mAh g}^{-1}$ , respectively. The specific capacities are gradually approaching to the theoretical capacity of silicon with extended reduction times from 4 h to 8 h and 16 h. This finding suggests that the improved capacities from HCl-4h to HCl-8h and HCl-16h not only originate from the increased the silicon content itself, but also from the modification of the fundamental electrochemical process. In addition, the ICE values of the HCl-4h, HCl-8h and HCl-16h samples increase from 37.8 % to

62.2 %, and 69.4 %. The inferior ICE value of the HCl-4h sample is consistent with the CV profile, where a strong peak from the formation of the SEI film is observed in the first cycle. The low ICE is likely due to the presence of silicon sub-oxide species because of limited reduction of silica by the short reduction time<sup>50-52</sup>. As compared to the HCl-4h sample, the ICE values of the HCl-8h and HCl-16h samples are significantly improved. The increased reduction time helps to promote the reduction of silica to form silicon, where less silicon sub-oxide species are left during the reduction process. It is worth pointing out that the HCl-8h and HCl-16h samples possess much higher specific surface area than the HCl-4h sample, which is normally detrimental to ICE. The results suggest that applying reduction time long enough is crucial to effectively convert silica to silicon and improve the ICE. The plateau of the HCl-4h sample decreases rapidly and the capacities decreases fast to nearly zero from the 2<sup>nd</sup> cycle, indicating poor structure and electrochemical stability<sup>53</sup>. The other samples exhibit similar discharge/charge patterns over cycles, where the plateaus are gradually shortened, and capacities are continuously decreased along with increasing cycles.

**Table 2.** Summarized property of the “HCl-washing” silicon, commercial  $\mu\text{m}$ -sized Si and literature data

Samples	1st discharge/charge capacity (mAhg <sup>-1</sup> )	1st CE (%)	Reversible capacity of 100 <sup>th</sup> cycle (mAhg <sup>-1</sup> )	Capacity retention of 100 <sup>th</sup> cycle (%)	Si content (%)	Ref
HCl-4h	499/189	37.8	13	6.9	33	this work
HCl-8h	975/606	62.2	143	23.6	40	this work
HCl-16h	1562/1084	69.4	812	74.9	55	this work
$\mu\text{m}$ -sized Si	3524/2930	83.1	10	0.3(50cycles)	100	this work
n <sub>p</sub> n-Si	1757/2748	64	1200	68	100	Ref 9
porous Si-650°C	1770	~68.5	1078	61	~58	Ref 30
porous Si-750°C	2080	~77.5	853	41	~64	Ref 30
hp-SiNSs	/	52	1800	/	100	Ref 36

**Table 3.** Summarized property of the “HF-etching” Si, commercial nano-sized Si

Samples	1st discharge/charge capacity (mAhg <sup>-1</sup> )	1st CE (%)	Reversible capacity of 200 <sup>th</sup> cycle (mAhg <sup>-1</sup> )	Capacity retention of 200 <sup>th</sup> cycle (%)	Si content (%)	Ref
HF-4h	2717/1700	62.5	1078	63.4	100	this work

HF-8h	2865/1850	64.6	1042	56.4	100	this work
HF-16h	3073/2005	65.2	984	49.0	100	this work
nano-sized Si	2912/2226	76.4	524	23.5	100	this work

The initial discharge and charge capacities of the HF-4h sample are 2717 mAh g<sup>-1</sup> and 1700 mAh g<sup>-1</sup>, respectively, giving an ICE of 62.5 %. Both the initial discharge/charge capacities and ICE are much higher than those of the HCl-4h sample. The removal of residual silica species significantly improves the electrochemical performance, particularly the ICE value, because there is only silicon present after HF etching. Correspondingly, the HF-8h silicon delivers increased initial discharge and charge capacities of 2865 mAhg<sup>-1</sup> and 1850 mAhg<sup>-1</sup>, respectively, with a slightly improved ICE of 64.6 %. As compared to the HF-4h and HF-8h silicon electrodes, the HF-16h silicon exhibits the highest initial coulombic efficiency of 65.2 %, with the initial discharge and charge capacities of 3073 mAhg<sup>-1</sup> and 2005 mAhg<sup>-1</sup>, respectively. The results prove that the extended reduction time improves the capacity and initial coulombic efficiency of the pure silicon electrode obtained after HF etching. The increased capacity of the three HF-etching samples is caused by the increased specific surface area which enhances the lithiation process. However, the slightly increased specific surface area does not promote the side reactions significantly, where the irreversible capacities do not change significantly. As a result, the ICE is slightly increased from the HF-4h to HF-8h and HF-16h samples. However, the HF-16h sample exhibits slightly lower ICE than the HCl-16h sample. This can be explained by the higher lithiation extent of HF-16h sample. The initial lithiation capacity of the HF-16h sample is 3073 mAhg<sup>-1</sup>, which is at least 8% higher than the actual lithiation capacity realized by silicon in the HCl-16 sample. As a result, larger volume expansion of the HF-16h electrode is expected compared to the HCl-16h electrode. The fresh electrode surface induced by volume expansion is exposed to electrolyte, which induces additional reaction with electrolyte and lithium consumption to form SEI layer. The ICE of the HF-16h sample is consequently compromised. The compromised ICE values are comparable to the reported work on the porous silicon synthesized via magnesiothermic reduction of SiO<sub>2</sub> under

similar conditions<sup>29, 34</sup>. Similar discharge/charge profiles are observed with all the HF-etching samples along with extended cycles, where lithiation and delithiation plateaus are still well retained after 100 cycles. It indicates a good structure and electrochemical stability of the porous silicon electrodes.

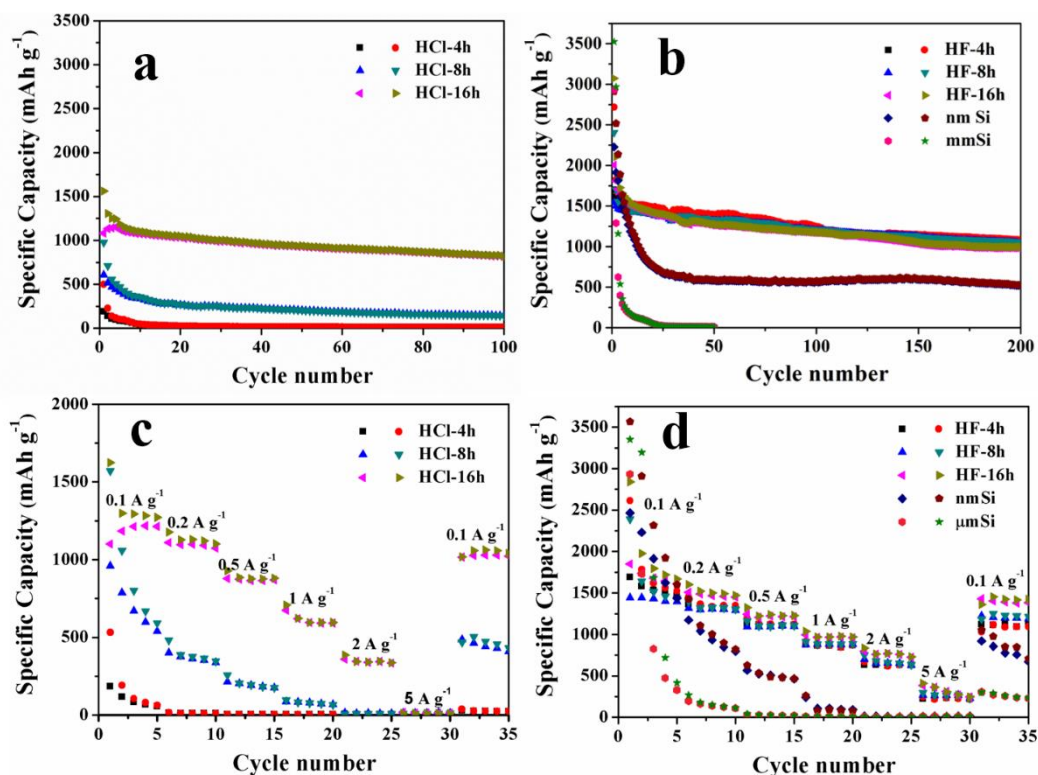


**Figure 3.** Cycling (a, b, current density: 0.2 A g<sup>-1</sup>) and rate (c, d) performance of the HCl-washing samples (a, c) and HF etching samples (b, d). The performance of the commercial nano-sized silicon particles and μm-sized silicon particles are also displayed in image b and d.

**Figure 3a** and **3b** show the overall cyclic performance of the HCl-washing and HF-etching silicon electrodes. The HCl-4h silicon electrode shows the fastest capacity fading rate, which reaches 45 mAh g<sup>-1</sup> after just 10 cycles and 13 mAh g<sup>-1</sup> after 100 cycles (Table 2). The poor cyclic stability is due to the presence of large amount of partially-reduced silica. The HCl-8h presents improved cyclic performance with the initial charge capacity of 606 mAh g<sup>-1</sup> and capacity retention of 23.6 % after 100 cycles. The HCl-16h silicon electrode shows the best cycling performance among the “HCl-washing” samples with the initial charge capacity of 1084 mAh g<sup>-1</sup> and capacity

retention of 74.9 % after 100 cycles, which is 812 mAh g<sup>-1</sup>. Both the imaging results (SEM and TEM) and porosity characterizations of the HF-etching samples suggest that macro-/mesoporous silicon structures are already formed within the HCl-washing samples synthesized with the reduction time of 4 h, 8 h and 16 h. Therefore, the improved cyclic stability of the HCl-washing samples with increased reduction time likely originates from the continuously decreased amount of the residual silica. The residual silica is detrimental for the porous silicon network to accommodate volume change and release mechanical stress, leading to deteriorated cyclic performance. Besides, the silica also inhibits electrolyte wetting and charge carrier transportation during the lithiation/delithiation process, leading to reduced absolute capacities. Therefore, the gradually decreased amount of silica enables the porous silicon with increased absolute capacities and improved cyclic performance.

As compared to the HCl-washing samples, the HF-etching silicon electrodes generally show a higher capacity and better cycling performance as seen in Figure 3b. The charge capacity of the HF-4h, HF-8h and HF-16h samples is around 1700 mAh g<sup>-1</sup>, 1850 mAh g<sup>-1</sup> and 2005 mAh g<sup>-1</sup> at the first cycle, and 1078 mAh g<sup>-1</sup>, 1042 mAh g<sup>-1</sup> and 984 mAh g<sup>-1</sup> after 200 cycles, with the capacity retention of 63.4%, 56.4 % and 49.0%, respectively. The significantly improved electrochemical performance of the HF-etching samples mainly originates from the removal of residual silica. The HF-etching process liberates macropores within the silicon, which is originally occupied by the residual silica particles. The macropores can effectively accommodate volume change of the silicon upon lithiation and delithiation, where the cyclic performance is drastically enhanced. Furthermore, the removal of the residual silica also promotes the electrolyte wetting on the silicon and facilitates the charge carrier transportation process, leading to increased absolute capacities. Considering that the mass loading density of the electrode is above 1 mg cm<sup>-2</sup> with respect to the silicon, the cyclic stability is quite good. Furthermore, it is worth pointing out that the cyclic performance of the HF-etching samples is even much better than those of the commercial nano-sized (average diameter:



30 nm) and micrometer sized silicon (size range: 2  $\mu\text{m}$  – 10  $\mu\text{m}$ ). The reversible capacity of the nano-sized silicon is only around 524  $\text{mAh g}^{-1}$  after 200 cycles and the micrometer silicon exhibits a capacity of nearly zero after only 50 cycles. The nano-sized silicon exhibits lower ICE and better cyclic performance than the large sized silicon due to its high specific surface area and small size feature<sup>13, 54-55</sup>. The apparently improved cyclic performance of the as-synthesized silicon addressed in this work indicates that the creation of hierarchical macro-/mesoporous within the silicon can bring better electrochemical performance than reducing particle size. Furthermore, considering that the size of the macro-/mesoporous silicon is in the range of micrometer scale, the results clearly prove that the existence of the macro-/mesoporous structures plays a crucial role in the electrochemical performance improvement. Besides, the micrometer size of the macro-/mesoporous silicon can also ensure the energy density due to its higher tap density ( $0.42 \text{ g cm}^{-3}$ ) than that of commercial nano-sized materials ( $0.18 \text{ g cm}^{-3}$ ). It seems that the initial discharge/charge capacities of the samples after HF etching are increased along with extended reduction time. However, the reversible capacities of the three samples are generally similar after 100 cycles. The increased initial capacities are ascribed to the slightly increased specific surface area from 4 h to 8 h and 16 h, where a gradually decreased initial coulombic efficiency is also observed. The gradually decreased capacity retention indicates that the structure details including pore size and wall thickness play an important role in the cyclic stability. Porous structure with thin wall and large pore diameter is more beneficial for increasing the capacity retention.

The rate capability of the HCl-washing samples at different current densities is shown in Figure 3c. The HCl-4h shows the worst rate performance, where the capacity drops to near zero from 0.2  $\text{A g}^{-1}$ . When the current density is reversed back to 0.1  $\text{A g}^{-1}$ , the capacity is still retained at around zero. The HCl-8h electrode displays reversible capacities of 959  $\text{mAh g}^{-1}$ , 401  $\text{mAh g}^{-1}$ , 215  $\text{mAh g}^{-1}$ , 87  $\text{mAh g}^{-1}$ , 13  $\text{mAh g}^{-1}$  and 12  $\text{mAh g}^{-1}$  at rates of 0.1  $\text{A g}^{-1}$ , 0.2  $\text{A g}^{-1}$ , 0.5  $\text{A g}^{-1}$ , 1  $\text{A g}^{-1}$ , 2  $\text{A g}^{-1}$  and 5  $\text{A g}^{-1}$  respectively. However, the capacity is recovered to only half of the initial value (485

mAh g<sup>-1</sup>) when the current density is reversed back to 0.1 A g<sup>-1</sup> from 5 A g<sup>-1</sup>. The HCl-16h silicon electrode presents the best rate performance among the three HCl-washing samples, which delivers capacities of 1100 mAh g<sup>-1</sup>, 1109 mAh g<sup>-1</sup>, 878 mAh g<sup>-1</sup>, 674 mAh g<sup>-1</sup>, 361 mAh g<sup>-1</sup> and 16 mAh g<sup>-1</sup> under the same testing condition. And the capacity is almost recovered to the initial value (1016 mAh g<sup>-1</sup>) when the current density is reversed back to 0.1 A g<sup>-1</sup> from 5 A g<sup>-1</sup>, indicating a better cyclic stability. The slight difference of the recovered capacity compared to the pristine value originates from moderate cyclic stability of the HCl-6h silicon. The good rate performance of the HCl-16h silicon is ascribed to the reduced amount of less electrochemically active residual silica related species, which is detrimental for electrochemical kinetics.

Figure 3d shows the rate performance of the HF-etching samples. The HF-etching samples show much better rate performance than the corresponding HCl-washing samples. The removal of the residual silica by the HF etching treatment significantly improves the electrochemical kinetics. The HF-4h electrode delivers capacities of 1690 mAh g<sup>-1</sup>, 1361 mAh g<sup>-1</sup>, 1123 mAh g<sup>-1</sup>, 879 mAh g<sup>-1</sup>, 632 mAh g<sup>-1</sup> and 226 mAh g<sup>-1</sup> at current density of 0.1 A g<sup>-1</sup>, 0.2 A g<sup>-1</sup>, 0.5 A g<sup>-1</sup>, 1 A g<sup>-1</sup>, 2 A g<sup>-1</sup> and 5 A g<sup>-1</sup> respectively. The capacity recovers to 1123 mAh g<sup>-1</sup> when the current density is reverted back to 0.1 A g<sup>-1</sup>. The HF-8h silicon electrode shows similar rate performance to the HF-4h sample. Unlike the HF-4h and HF-8h silicon electrodes, the HF-16h one exhibits an improved rate performance. The specific charge capacity of the HF-16h sample at 0.1 A g<sup>-1</sup> is 1850 mAh g<sup>-1</sup>. As the current density increases, a specific capacity of 1510 mAh g<sup>-1</sup>, 1245 mAh g<sup>-1</sup>, 995 mAh g<sup>-1</sup>, 799 mAh g<sup>-1</sup> and 383 mAh g<sup>-1</sup> is obtained with increasing current densities. Furthermore, a high reversible capacity of 1431 mAh g<sup>-1</sup> is recovered when the current density is reversed back to 0.1 A g<sup>-1</sup>. The better rate performance of the HF-16h sample is due to its higher specific surface area than the other two samples, which facilitates electrolyte wetting and charge carrier transportation. Furthermore, all the HF-etching samples exhibit a clearly improved rate performance as compared with the commercial nano-sized and micrometer silicon particles. The results suggest that the 3D

hierarchical macro-/mesoporous structures effectively improve the electrochemical kinetics, even though the size of the as-synthesized porous silicon is in the micrometer range.

**Figure 4a** depicts the Nyquist plots of the HCl-4h, HCl-8h and HCl-16h silicon electrodes after 20 cycles. The three samples all exhibit two semi-circles in the high-to-medium frequency region and one slope in the low frequency region. According to the equivalent circuit, the total cell resistance ( $R_S+R_{SEI}+R_{CT}$ ) of the samples HCl-4h, HCl-8h and HCl-16h is 196  $\Omega$ , 135  $\Omega$  and 120  $\Omega$ , respectively. The decreased resistance with increasing reduction time originates from the gradually increased BET surface area and the decreased content of the less electrochemically active silicon oxide related species. The result is consistent with the rate performance of the HCl-washing samples.

The Nyquist plots of the HF-4h, HF-8h and HF-16h samples are displayed in resistance. One depressed semicircle is observed in the high frequency range together with a slope in the low frequency region. The different patterns of the HF-etching silicon compared to the HCl washing samples are related to the removal of the silica species by HF etching. It is well accepted the depressed semicircle in the high-frequency range stands for charge transfer impedance ( $R_{ct}$ ), while the inclined line in the low frequency range are corresponding to the Warburg impedance owing to the ion diffusion-controlled process<sup>56-58</sup>. Based on the equivalent circuit model presented in the inset of Figure 4b, the  $R_{ct}$  of the HF-4h, HF-8h and HF-16h electrodes after 20cycles is fit to be 69.9  $\Omega$ , 51.3  $\Omega$  and 46.5  $\Omega$ , respectively. The gradual decrease of the  $R_{ct}$  value along with increasing reduction time originates from the gradually increased BET surface area and increased portion of mesopores. Besides, the EIS profile as a function of cycle number is also investigated in order to compare the cyclic stability of the HCl-washing sample and HF-etching sample. According to the fitting results based on the equivalent circuit models, the total cell resistance values ( $R_S+R_{SEI}+R_{CT}$ ) of the HCl-16h electrode are fit to be 111  $\Omega$ , 120  $\Omega$  and 180  $\Omega$  after 10, 20, and 50 cycles respectively. The gradually increasing resistance indicates a moderate cyclic stability of the HCl-16h sample. Figure 4d shows the diameter of the depressed semicircle in the high-frequency range for the HF-16h,

which is almost identical after different cycles. Specifically, the  $R_{ct}$  values of the HF-16h electrodes after 10, 20, and 50 cycles are fit to be  $42.8\ \Omega$ ,  $46.5\ \Omega$  and  $47.2\ \Omega$ , indicating good cyclic stability of HF-16h sample.

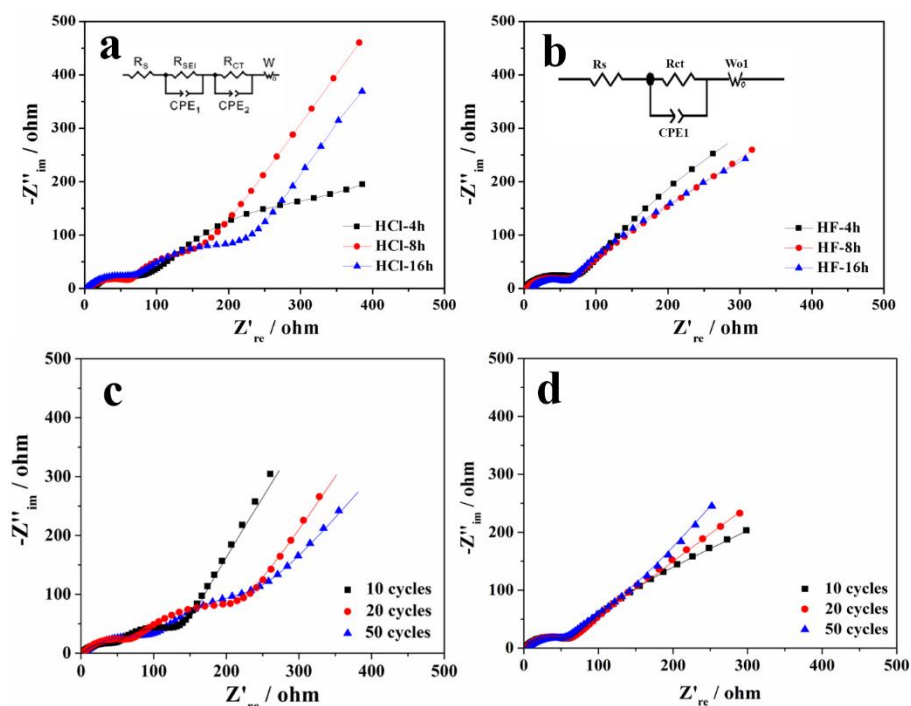


**Figure 4.** (a, b) Nyquist plots and model circuit (inset) of porous silicon after 20 charge/discharge cycles at a current density of  $0.2\ \text{A g}^{-1}$ ; (c, d) Nyquist plots of porous silicon after different cycles for HCl-16h (c) and HF-16h (d).

To investigate the structure stability of the porous silicon electrode upon lithiation and delithiation, the dimensional changes of the HF-4h electrode after 10 cycles are characterized using cross-section SEM (**Figure 5**). After lithiation at the 10<sup>th</sup> cycle, the thickness of HF-4h electrode is expanded by 136 % compared to the pristine electrode ( $56\ \mu\text{m}$  vs.  $41\ \mu\text{m}$ ). After delithiation at the 10<sup>th</sup> cycle, the thickness is decreased to  $51\ \mu\text{m}$ , which is partially restored to the original thickness in the pristine electrode. The cross-section SEM image results indicate that the HF-4h electrode possesses good structure stability over cycles, which is comparable with some reported work on the porous silicon<sup>59-60</sup>. Besides, no visible cracks are

observed on the surface of the cycled electrode of the HF-4h, while big cracks appear in the HCl-4h electrode (Figure S8). These results indicate that hierarchical porous structure plays an active role in buffering against the volume change and the good cycling stability of the HF-4h electrode is closely related to its robust structure during cycling.

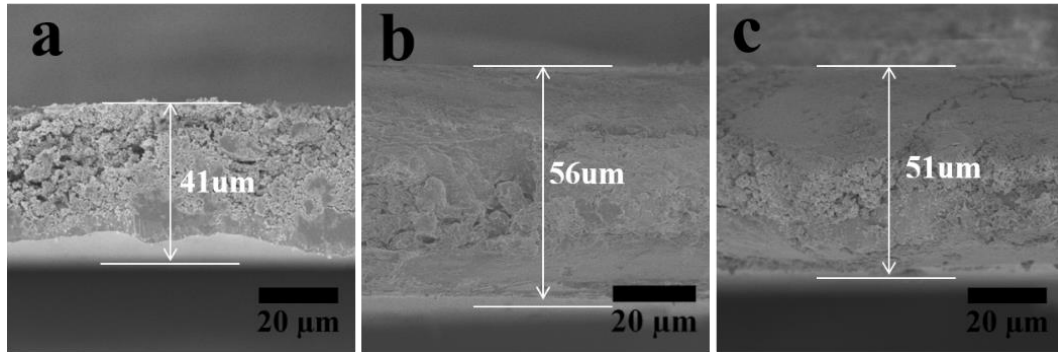


**Figure 5.** Cross-sectional SEM images of HF-4h electrode after 10 cycles. (a) pristine, (b)full lithiation state, (c) delithiation state.

Besides the experimental investigation on the structure and properties, theoretical simulation via finite element analysis is also applied to reveal the structure-property correlation of the porous silicon. There have been some relevant simulation studies addressing the merits of porous silicon during lithiation<sup>45, 47, 61</sup>. However, to our best knowledge, no work has been reported about the mechanical deformation mechanism of the particular porous structure addressed in this work, where pore size and wall thickness are varied systematically, while the sum of the pore diameter and wall thickness keeps constant. The correlation between the structure variation and mechanical response including spatial stress distribution, strain and displacement change are revealed with different lithiation extents. The normalized lithium concentration is surrogated by temperature, and the lithiation expansion coefficient of  $\beta_{ij}$  is equivalently treated as the thermal expansion coefficient. For simplicity, it is assumed that the coefficient  $\beta_{ij}$  is isotropic, that is,  $\beta_{ij} = \beta \delta_{ij}$ . The lithium and stress-strain fields are solved with an implicit large deformation procedure in ABAQUS/Standard. A representative volume element (RVE) is used

to model stress generation during lithiation and the lithium concentration is assumed to vary simultaneously in the RVE.

An elastic and perfect plastic model is adopted to evaluate the deformation and stress states during lithiation of the electrode<sup>62-63</sup>. The total strain rate  $\dot{\varepsilon}_{ij}$  is taken to be the sum of three contributions

$$\dot{\varepsilon}_{ij} = \dot{\varepsilon}_{ij}^e + \dot{\varepsilon}_{ij}^p + \dot{\varepsilon}_{ij}^c \quad (1)$$

where  $\dot{\varepsilon}_{ij}^e$  is the elastic strain rate  $\dot{\varepsilon}_{ij}^p$  the plastic strain rate and  $\dot{\varepsilon}_{ij}^c$  the chemical strain rate or the lithiation-induced strain rate. In Eq. (1), the elastic strain rate  $\dot{\varepsilon}_{ij}^e$  obeys Hooke's law:

$$\dot{\varepsilon}_{ij}^e = \frac{1}{E} [(1 + \nu)\dot{\sigma}_{ij} - \nu\dot{\sigma}_{kk}\delta_{ij}] \quad (2)$$

where  $E$  is Young's modulus,  $\nu$  is Poisson's ratio,  $\delta_{ij}$  is Kronecker symbol ( $\delta_{ij}=1$  when  $i=j$  and  $\delta_{ij}=0$  otherwise), and repeats indices meant summation.

When the effective stress  $\sigma_{eq}$  equals the yield strength  $\sigma_y$ , that is  $\sigma_{eq} = \sigma_y$ , plastic yielding occurs. In Eq. (1), the plastic strain rate  $\dot{\varepsilon}_{ij}^p$  obeys the classic  $J2$ -flow rule:

$$\dot{\varepsilon}_{ij}^p = \lambda s_{ij} \quad (3)$$

where  $s_{ij} = \sigma_{ij} - \sigma_{kk}\delta_{ij}/3$  is the deviatoric stress and  $\sigma_{eq} = \sqrt{3s_{ij}s_{ij}/2}$  the equivalent stress. Within the perfect plastic model,  $\lambda$  is a positive scalar at each increment to be determined by the boundary-value problem.

In Eq. (1), the chemical strain rate  $\dot{\varepsilon}_{ij}^c$  is caused by lithiation and is proportional to the rate of the normalized Li concentration

$$\dot{c}\dot{\varepsilon}_{ij}^c = \beta_{ij}\dot{c} \quad (4)$$

Where  $\beta_{ij}$  is the lithiation expansion coefficient, and  $c$  varies between 0 (pristine Si) and 1 (fully lithiated  $\text{Li}_{3.75}\text{Si}$ ).

A close packing structure model of the porous silicon is established as seen in **Figure 6**. To simplify the calculation, the silicon network is set as mesopore-free. The parameters of the wall thicknesses and pore sizes are defined by both the experimental and arbitrary values (**Table 4**), where clear trends regarding the

mechanical deformation behaviour are given by the finite element analysis. The boundary condition is defined as following: An isotropic volume expansion is assumed with respect to each representative volume element (RVE). 1/8 of the RVE is chosen as a structure model to conduct simulation. Symmetric boundary condition is applied on the symmetric face. The displacement of the side face and the direction vertical to the side face is defined as zero. The top surface is free for expansion. The mesh size is defined based on a balance between resolution and load of simulation. For example, the minimum and maximum size of the element length is 8 nm and 18.6 nm respectively in the structure model I.

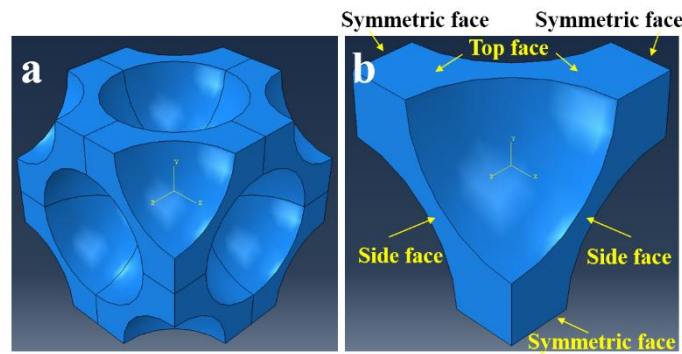


**Figure 6.** Structure model of porous silicon used for the finite element analysis. Details: (a) construction unit of the 3D porous silicon, (b) a representative volume element.

**Table 4.** Structural parameters of the porous silicon model structures used for finite element analysis

Structure model	Cube edge (a/nm)	Pore diameter (D/nm)	Wall thickness (t/nm)
I	600	400	25
II	600	381	37
III	600	352	69
IV	600	339	87
V	600	300	125

Different representative lithiation states as indicated by the volume change ratio of 150 %, 200 %, 250 % and 300 % against the pristine volume of the silicon are analysed<sup>44</sup>. Other parameters utilized to perform the finite element analysis are listed in **Table 5**. The thermal coefficient used in the simulation is calculated based on the volume expansion rate in Eq.(5), where the initial strain value is derived by choosing  $\Delta T$  value of 1 K and  $\beta$  value from Table 5 according to Eq.(6)<sup>64</sup>.

$$\beta = \sqrt[3]{\Lambda} - 1 \quad (5)$$

$$\varepsilon_0 = \beta \Delta T \quad (6)$$

**Table 5.** Critical parameters of the porous silicon utilized for finite element analysis

Volume expansion rate ( $\Lambda$ )	Regularized nominal lithium concentration (C)	Modulus (E/GPa)	Thermal expansion coefficient ( $\beta$ )	Yield limit ( $\sigma_y$ /MPa)
150 %	1.875	62.6	0.1447	2000
200 %	2.500	50.0	0.2599	2000
250 %	3.125	37.5	0.3572	2000
300 %	3.750	25.0	0.4422	2000

The distribution of the stress, strain, and displacement of the model structure II corresponding to the HF-4h sample is displayed in **Figure 7**(magnified scale bars presented in Figure S9). The stress distribution results in Figure 7a, 7d, 7g and 7j indicate that high stress is generated in the shell region of the macropores, which reaches the yield limit with 150 % of the volume change ratio. However, the stress level of the boundary regions between the macropores is relatively low. The mechanical stress distributed in the boundary area is gradually increased along with increasing volume ratio from 150 % to 300 %, but it still much smaller than the values over the shell region of the macropores. It implies that the boundary region between the neighbouring macropores is stabilized during the lithiation process, which is beneficial for retaining the macroporous structure and therefore achieve good cyclic stability.

The corresponding equivalent plastic strain (PEEQ) change in Figure 7b, 7e, 7h and 7k shows that the strain is gradually increased when the lithiation process proceeds. The high strain mainly occurs in the shell region of the macropores, where the boundary region between the neighbouring macropores exhibits minimum strain. The displacement evolution of the porous silicon with the model structure II is demonstrated in Figure 7c, 7f, 7i and 7l, which is increased with the volume change ratio from 150 % to 300 %. The displacement near the free surface is much larger than other region, and the largest displacement occurs at the place within the thinner wall.



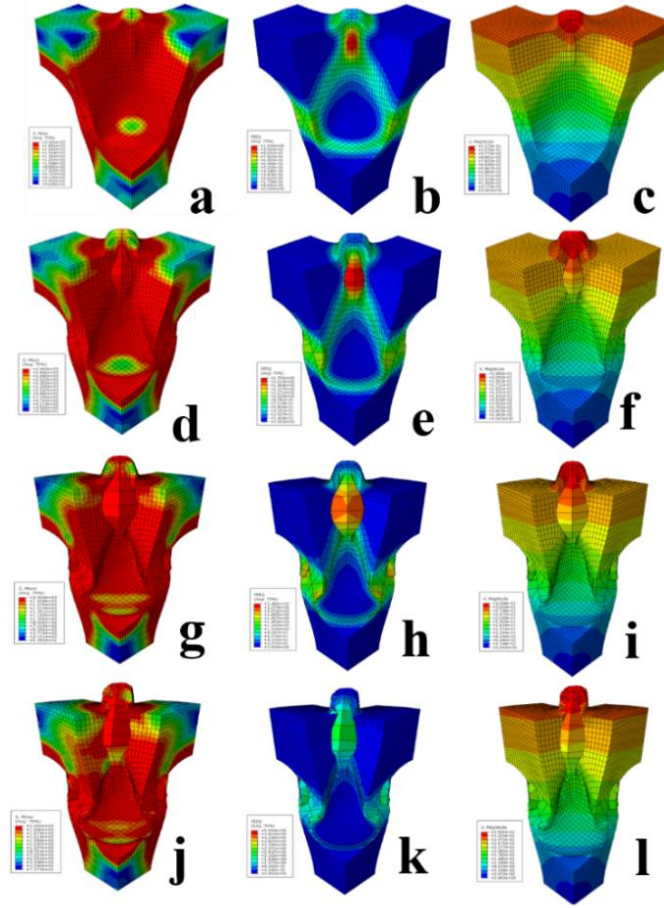


**Figure 7.** Stress (a, d, g, j), strain (b, e, h, k) and displacement (c, f, i, l) distribution of porous silicon calculated with the model structure II along with increasing volume change ratio. Volume expansion ratios are 150 % (a, b, c), 200 % (d, e, f), 250 % (g, h, i), and 300 % (j, k, l).

The distribution of stress, strain, and displacement of the porous silicon with the model structure III corresponding to the HF-8h sample is exhibited in Figure S10. Similar with the porous silicon with larger pore size and thinner wall (model structure II), high stress is generated in the shell regions of the macropores, where the boundary area between the neighbouring macropores has much less stress. Along with increasing lithiation degree, the stress gradually increases in the boundary regions, but the values are still quite limited compared to the stress observed in the shell areas of the macropores. Besides, the strain of the model structure III is increased with increasing volume change ratio as expected and the displacement field shows similar deformation behaviour with the model structure II.

With the pore size further decreased and wall thickness increased (model structure IV), the stress of the porous silicon upon lithiation becomes pronounced even in the boundary region between the neighbouring macropores (Figure S11). It seems that the boundary region with small stress is reduced significantly with increasing volume change ratio from 150 % to 200 %, 250 %, and 300 %. The strain is increased compared to the porous silicon with the model structure III at different volume change ratios. However, the displacement is less pronounced than that of the model structure III at each individual volume change ratio.

The stress distribution of the porous silicon with different pore sizes and wall thicknesses at different volume change ratio is compared in **Figure 8** (magnified scale bars presented in Figure S12). When the volume change ratio is 150 %, as shown in Figure 8a, 8e, 8i, 8m and 8q, the stress generated at the boundary region between the neighbouring macropores is increased from the model structure I to II, III, IV and V where the area of the boundary region with small stress is reduced simultaneously. The reduced stress is ascribed to the macropores with a large pore size, which effectively alleviates the stress upon lithiation, particularly at the boundary regions between neighbouring macropores. The results elucidate the critical role of the macropores for stress mitigation and structure stabilization of the porous silicon during the lithiation process.

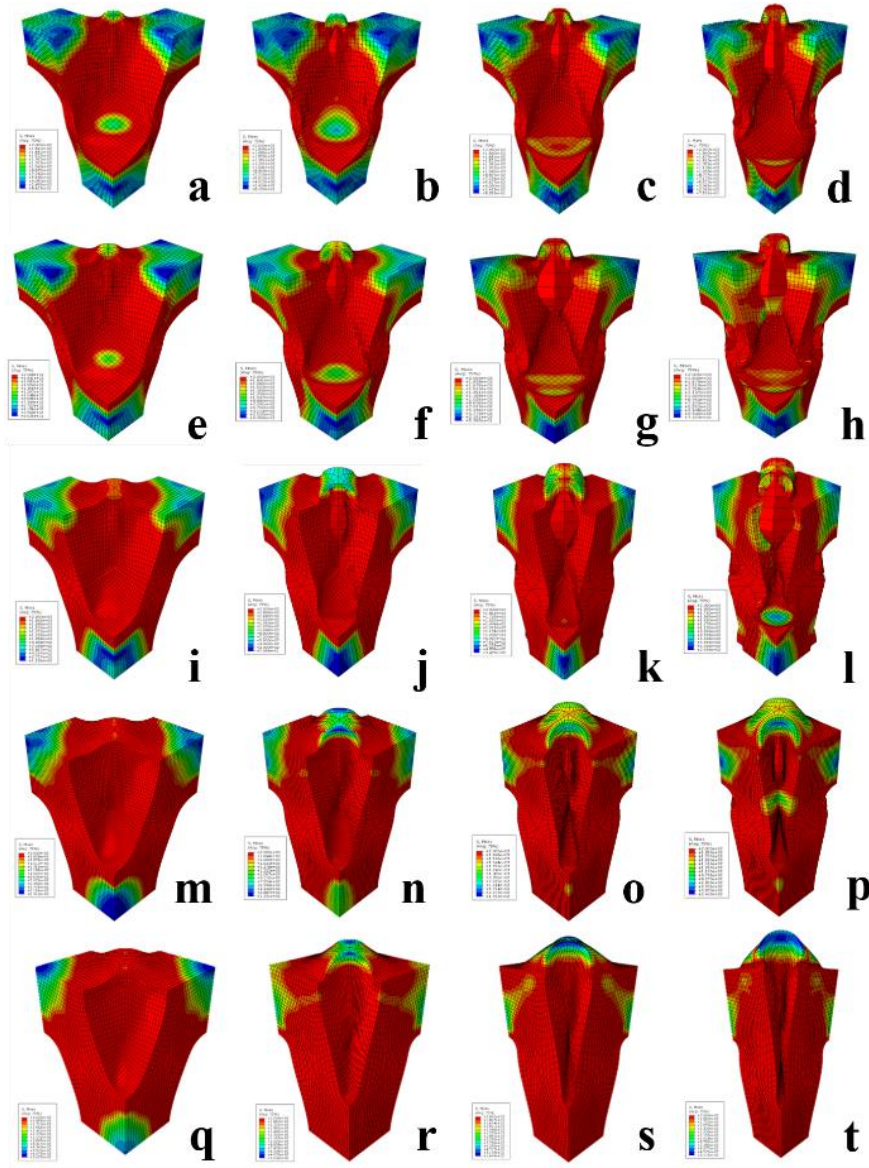


**Figure 8.** Stress distribution of porous silicon calculated with the model structure I (a, b, c, d), II (e, f, g, h), III (i, j, k, l), IV (m, n, o, p), V (q, r, s, t) along with increasing volume change ratio. Details: 150 % (a, e, i, m, q), 200 % (b, f, j, n, r), 250 % (c, g, k, o, s), and 300 % (d, h, l, p, t).

The same trend is observed when the volume change ratio is increased from 150 % to 200 %. The change of the stress distribution is even more drastic compared to that of the situation with the volume change ratio of 150 %. It further implies that the increase of the wall thickness and decrease of the pore size in the porous silicon significantly increase the stress in the boundary region as the lithiation process proceeds. When the volume change ratio is increased to 250 % and 300 %, even the boundary region of the porous silicon with the largest pore size and thinnest wall thickness (model

structure I) exhibits significantly increased stress. It indicates that the high stress generated in the shell of the macroporous silicon spreads to the boundary region along with extended lithiation. The areas of the boundary regions with less stress become limited with the volume change ratio of 250 % and 300 % with respect to the porous silicon with reduced pore sizes and thickened walls (model structure II, III, IV and V). The evolution of strain in different lithiation extent suggest that the increased pore size and decreased wall thickness can lower the stress level, which is beneficial for structure stabilization of the porous silicon.

Like the evolution trend of the stress, the change of the strain distribution in porous silicon with decreased pore sizes and thickened wall thicknesses at different lithiation states is also pronounced as indicated by **Figure S13** (magnified scale bars presented in Figure S14). The strain generated in the shell of the macroporous silicon is significantly increased from the model structure I to the model structure II, III, IV and V with the same volume change ratios. The results suggest that the porous silicon with small pore size and large wall thickness possesses larger strain during the lithiation process compared to the porous silicon with increased pore size and reduced wall thickness. The large pore size provides more space for the volume change of the silicon wall at different lithiation degrees, leading to decreased strain. When the pore size is reduced together with increased wall thickness, the space provided by the macropores to accommodate the volume expansion of the silicon wall is decreased. As a result, the strain is enlarged correspondingly at all lithiation states and the largest strain is observed with the model structure V at all lithiation states.

With respect to the displacement evolution behavior of the porous silicon with the gradually decreased pore sizes and increased wall thicknesses (**Figure S15**, magnified scale bars presented in Figure S16), it seems that decreasing the pore sizes can generate larger displacement in the vertical direction under the same volume change ratio. The macroporous silicon with large pore size has more space to accommodate volume change, thus leading to less longitudinal displacement, and vice versa.

In a brief summary, a clear trend is shown by the finite element analysis, where the porous silicon with larger pore diameter and thinner wall thickness generate less stress, reduced strain, and decreased displacement. The shoulder regions of the porous silicon display less stress and strain than the shell areas, which are still gradually increased with increasing lithiation extent. The displacement takes place mainly along the vertical direction, which also becomes pronounced with enlarged volume change ratios. The lower stress and strain exhibited by increased pore size and decreased wall thickness help to stabilize the electrode, leading to improved cyclic performance. The mechanical simulation results provide a clear principle towards structure design and synthesis of high performance porous silicon anode.

## CONCLUSIONS

A strategy to synthesize 3D hierarchical macro-/mesoporous silicon with tunable pore size and wall thickness has been successfully developed. By applying a series of different reaction time on the magnesiothermic reduction process of the 0D Stöber silica particles, a systematic control over the morphology, structure and porosity is achieved. The structures of the macro-/mesoporous silicon synthesized with the reduction time of 4 h, 8 h, and 16 h, and different post-treatment methods (HCl washing only, or followed by HF etching) are systematically characterized by various techniques. The mechanism for the morphology evolution of the 3D hierarchical macro-/mesoporous silicon is proposed. A self-templating process is governing the construction of the macro-/mesoporous silicon, where silica particles act as templating agents and precursor for the silicon simultaneously. The gradually enhanced conversion from silica to silicon with increased reduction time introduces morphology and structure changes affecting the pore diameter, wall thickness, and porosity. Particularly, the pore diameter is gradually decreased, while the wall thickness is thickened with increased reduction time. The sum of the pore diameter and wall thickness almost remains constant. Regarding the HCl-washing sample series, the reduction time of 16 h brings the best electrochemical performance including absolute reversible capacities, cyclic stability, and rate performance as

compared to the reaction time of 4 h and 8 h. One of the major reasons responsible for the significant performance improvement of the HCl-washing sample series is the enhanced conversion from silica to silicon by an increased reduction time. Concerning the HF-etching samples, firstly, the electrochemical performance of all the samples is clearly improved after HF etching due to removal of residual silica. Secondly, the initial discharge/charge capacities are increased with extended reduction time. However, the reversible capacities after 100 cycles are similar among the samples with different reduction times. It indicates that the increased reduction time reduces the capacity retention of the HF-etching porous silicon samples, which is due to the structure change of the silicon. The capacity retention ratio is decreased with extended reduction time due to increased wall thickness and reduced pore diameter. Thirdly, the HF-16h sample exhibits improved rate performance compared with the HF-4h and HF-8h silicon electrodes due to its higher specific surface area. Finally, all the HF-etching samples exhibit a clearly improved cyclic and rate performance as compared to commercial nano-sized and micrometer silicon particles.

The finite element analysis indicates that the increase of the wall thickness and decrease of the pore size in the porous silicon significantly increase the stress in the boundary region as the lithiation process proceeds, which is unfavourable for structure stabilization and maintaining good cyclic performance. The porous silicon with small wall thickness and large pore size shows reduced stress, strain, and increased displacement. The finite element analysis provides an effective principle towards structure design of high-performance porous silicon anode.

## Supporting Information

Supporting Information is available from the ACS Publications website or from the author. SEM, TEM, HRTEM images and SAED pattern of the pristine SiO<sub>2</sub>; SEM images, XRD patterns, HRTEM images, SAED patterns, N<sub>2</sub> adsorption and desorption isotherms and corresponding BJH pore size distribution curves of the porous silicon; Cyclic voltammetry curves and Galvanostatic discharge/charge profiles of the porous silicon; Stress, strain and displacement distribution of the

porous silicon calculated with the model structure III, IV along with increasing volume change ratios.

## ACKNOWLEDGMENTS

This research is funded by the Natural Science Foundation of China (51702335), Zhejiang Province welfare technology applied research project (LGG19B010001), the Natural Science Foundation of Ningbo City (2018A610084), the CAS-EU S&T cooperation partner program (174433KYSB20150013), and Key Laboratory of Bio-based Polymeric Materials of Zhejiang Province. This project has received funding from the European Union's Horizon 2020 research and innovation program under the Marie Skłodowska-Curie grant agreement No 655881. S.Y. acknowledges the China Scholarship Council (CSC). P.M-B acknowledges funding by the International Research Training Group 2022 Alberta/Technical University of Munich International Graduate School for Environmentally Responsible Functional Hybrid Materials (ATUMS). P.G.B. is indebted to the Engineering and Physical Sciences Research Council (EPSRC), including the SUPERGEN Energy Storage Hub (EP/L019469/1), Enabling Next Generation Lithium Batteries (EP/M009521/1), Henry Royce Institute for Advanced Materials (EP/R00661X/1, EP/S019367/1, EP/R010145/1) and the Faraday Institution All-Solid-State Batteries with Li and Na Anodes (FIRG007, FIRG008) for financial support.

## REFERENCES

- (1) Liu, L.; Lyu, J.; Li, T.; Zhao, T. Well-Constructed Silicon-Based Materials as High-Performance Lithium-Ion Battery Anodes. *Nanoscale* **2016**, 8 (2), 701-722.
- (2) Casimir, A.; Zhang, H.; Ogoke, O.; Amine, J. C.; Lu, J.; Wu, G. Silicon-Based Anodes for Lithium-Ion Batteries: Effectiveness of Materials Synthesis and Electrode Preparation. *Nano Energy* **2016**, 27, 359-376.
- (3) Xu, Q.; Li, J.-Y.; Sun, J.-K.; Yin, Y.-X.; Wan, L.-J.; Guo, Y.-G. Watermelon-Inspired Si/C Microspheres with Hierarchical Buffer Structures for Densely Compacted Lithium-Ion Battery Anodes. *Adv. Energy Mater.* **2017**, 7 (3), 1601481.
- (4) Wu, H.; Cui, Y. Designing Nanostructured Si Anodes for High Energy Lithium Ion Batteries. *Nano Today* **2012**, 7 (5), 414-429.
- (5) Lee, J.; Moon, J.; Han, S. A.; Kim, J.; Malgras, V.; Heo, Y.-U.; Kim, H.; Lee, S.-M.; Liu, H. K.; Dou, S. X. Everlasting Living and Breathing Gyroid 3d Network in Si@ SiO<sub>x</sub>/C Nanoarchitecture for Lithium Ion

Battery. *ACS nano* **2019**,*13* (8), 9607-9619.

(6) He, L.; Tan, C.; Sheng, C.; Chen, Y.; Yu, F.; Chen, Y. A B-Feooh/Mxene Sandwich for High-Performance Anodes in Lithium-Ion Batteries. *Dalton Trans.* **2020**,*49* (27), 9268-9273.

(7) Sheng, C.; Zhang, C.; Shen, X.; Zhao, S.; Fu, L.; Wu, Y.; Wang, J.; Chen, Y. Sns2/N-Doped Graphene as a Superior Stability Anode for Potassium-Ion Batteries by Inhibiting "Shuttle Effect". *Batteries & Supercaps* **2020**,*3* (1), 56-59.

(8) Zuo, X.; Zhu, J.; Müller-Buschbaum, P.; Cheng, Y.-J. Silicon Based Lithium-Ion Battery Anodes: A Chronicle Perspective Review. *Nano Energy* **2017**,*31*, 113-143.

(9) Xiao, W.; Zhou, J.; Yu, L.; Wang, D.; Lou, X. W. Electrolytic Formation of Crystalline Silicon/Germanium Alloy Nanotubes and Hollow Particles with Enhanced Lithium-Storage Properties. *Angew. Chem.-Int. Edit.* **2016**,*55* (26), 7427-7431.

(10) An, W.; Gao, B.; Mei, S.; Xiang, B.; Fu, J.; Wang, L.; Zhang, Q.; Chu, P. K.; Huo, K. Scalable Synthesis of Ant-Nest-Like Bulk Porous Silicon for High-Performance Lithium-Ion Battery Anodes. *Nat. Commun.* **2019**,*10* (1), 1-11.

(11) Shivaraju, G.; Sudakar, C.; Prakash, A. High-Rate and Long-Cycle Life Performance of Nano-Porous Nano-Silicon Derived from Mesoporous Mcm-41 as an Anode for Lithium-Ion Battery. *Electrochim. Acta* **2019**,*294*, 357-364.

(12) Zhao, T.; Zhu, D.; Li, W.; Li, A.; Zhang, J. Novel Design and Synthesis of Carbon-Coated Porous Silicon Particles as High-Performance Lithium-Ion Battery Anodes. *J. Power Sources* **2019**,*439*, 227027.

(13) Feng, K.; Li, M.; Liu, W.; Kashkooli, A. G.; Xiao, X.; Cai, M.; Chen, Z. Silicon-Based Anodes for Lithium-Ion Batteries: From Fundamentals to Practical Applications. *Small* **2018**,*14* (8), 1613-6810.

(14) Yu, Y.; Gu, L.; Zhu, C.; Tsukimoto, S.; van Aken, P. A.; Maier, J. Reversible Storage of Lithium in Silver-Coated Three-Dimensional Macroporous Silicon. *Adv. Mater.* **2010**,*22* (20), 2247-50.

(15) Choi, S.; Bok, T.; Ryu, J.; Lee, J. I.; Cho, J.; Park, S. Revisit of Metallothermic Reduction for Macroporous Si: Compromise between Capacity and Volume Expansion for Practical Li-Ion Battery. *Nano Energy* **2015**,*12*, 161-168.

(16) Ashuri, M.; He, Q.; Shaw, L. L. Silicon as a Potential Anode Material for Li-Ion Batteries: Where Size, Geometry and Structure Matter. *Nanoscale* **2016**,*8* (1), 74-103.

(17) Unagami, T. Formation Mechanism of Porous Silicon Layer by Anodization in Hf Solution. *J. Electrochem. Soc.* **1980**, *127* (2), 476-483.

(18) Díaz-Torres, E.; Romero-Paredes, G.; Peña-Sierra, R.; Ávila-García, A. Formation and Characterization of Porous Silicon Films Obtained by Catalyzed Vapor-Chemical Etching. *Mater. Sci. Semicond. Process.* **2015**,*40*, 533-538.

(19) Azeredo, B. P.; Lin, Y.-W.; Avagyan, A.; Sivaguru, M.; Hsu, K.; Ferreira, P. Direct Imprinting of Porous Silicon Via Metal-Assisted Chemical Etching. *Adv. Funct. Mater.* **2016**,*26* (17), 2929-2939.



- (20) Li, C.; Zhang, P.; Jiang, Z. Effect of Nano Cu Coating on Porous Si Prepared by Acid Etching Al-Si Alloy Powder. *Electrochim. Acta* **2015**, *161* (0), 408-412.
- (21) Feng, J.; Zhang, Z.; Ci, L.; Zhai, W.; Ai, Q.; Xiong, S. Chemical Dealloying Synthesis of Porous Silicon Anchored by in Situ Generated Graphene Sheets as Anode Material for Lithium-Ion Batteries. *J. Power Sources* **2015**, *287*, 177-183.
- (22) He, W.; Tian, H.; Xin, F.; Han, W. Scalable Fabrication of Micro-Sized Bulk Porous Si from Fe-Si Alloy as a High Performance Anode for Lithium-Ion Batteries. *J. Mater. Chem. A* **2015**, *3* (35), 17956-17962.
- (23) Cao, W.; Han, K.; Chen, M.; Ye, H.; Sang, S. Particle Size Optimization Enabled High Initial Coulombic Efficiency and Cycling Stability of Micro-Sized Porous Si Anode Via Alsi Alloy Powder Etching. *Electrochim. Acta* **2019**, *320*, 134613.
- (24) Wang, X.; Wu, Y.; Liu, X.; Chen, J.; Zhen, C.; Ma, L.; Hou, D. A Template-Based Method for Preparing Ordered Porous Silicon. *J. Porous Mater.* **2015**, *22* (6), 1431-1435.
- (25) Jeong, J.-H.; Kim, K.-H.; Jung, D.-W.; Kim, K.; Lee, S.-M.; Oh, E.-S. High-Performance Characteristics of Silicon Inverse Opal Synthesized by the Simple Magnesium Reduction as Anodes for Lithium-Ion Batteries. *J. Power Sources* **2015**, *300*, 182-189.
- (26) Wu, H.; Du, N.; Shi, X.; Yang, D. Rational Design of Three-Dimensional Macroporous Silicon as High Performance Li-Ion Battery Anodes with Long Cycle Life. *J. Power Sources* **2016**, *331*, 76-81.
- (27) Yan, Z.; Guo, J. High-Performance Silicon-Carbon Anode Material Via Aerosol Spray Drying and Magnesiothermic Reduction. *Nano Energy* **2019**, *63*, 103845.
- (28) Gao, S. L.; Yang, D. D.; Pan, Y. Y.; Geng, L. Y.; Li, S. Q.; Li, X. H.; Cao, P. F.; Yang, H. B. From Natural Material to High-Performance Silicon Based Anode: Towards Cost-Efficient Silicon Based Electrodes in High-Performance Li-Ion Batteries. *Electrochim. Acta* **2019**, *327*, 9.
- (29) Entwistle, J. E.; Beaucage, G.; Patwardhan, S. V. Mechanistic Understanding of Pore Evolution Enables High Performance Mesoporous Silicon Production for Lithium-Ion Batteries. *J. Mater. Chem. A* **2020**, *8* (9), 4938-4949.
- (30) Jia, H.; Zheng, J.; Song, J.; Luo, L.; Yi, R.; Estevez, L.; Zhao, W.; Patel, R.; Li, X.; Zhang, J.-G. A Novel Approach to Synthesize Micrometer-Sized Porous Silicon as a High Performance Anode for Lithium-Ion Batteries. *Nano Energy* **2018**, *50*, 589-597.
- (31) Shivaraju, G. C.; Sudakar, C.; Prakash, A. S. High-Rate and Long-Cycle Life Performance of Nano-Porous Nano-Silicon Derived from Mesoporous Mcm-41 as an Anode for Lithium-Ion Battery. *Electrochim. Acta* **2019**, *294*, 357-364.
- (32) Duan, Y.-J.; Zhao, D.-L.; Meng, W.-J.; Yang, H.-X.; Han, X.-Y.; Tian, X.-M.; Zhao, M. Ordered Mesoporous Si Microspheres with Nitrogen-Doped Carbon Coating for Advanced Lithium-Ion Battery Anodes. *J. Alloys Compd.* **2019**, *800*, 198-207.
- (33) Zhao, Y.; Liu, X.; Li, H.; Zhai, T.; Zhou, H. Hierarchical Micro/Nano Porous Silicon Li-Ion Battery

Anodes. *Chem. Commun.* **2012**,48 (42), 5079-5081.

(34) Xiao, Q.; Gu, M.; Yang, H.; Li, B.; Zhang, C.; Liu, Y.; Liu, F.; Dai, F.; Yang, L.; Liu, Z.; Xiao, X.; Liu, G.; Zhao, P.; Zhang, S.; Wang, C.; Lu, Y.; Cai, M. Inward Lithium-Ion Breathing of Hierarchically Porous Silicon Anodes. *Nat. Commun.* **2015**,6, 8844.

(35) Cui, M.; Wang, L.; Guo, X.; Wang, E.; Yang, Y.; Wu, T.; He, D.; Liu, S.; Yu, H. Designing of Hierarchical Mesoporous/Macroporous Silicon-Based Composite Anode Material for Low-Cost High-Performance Lithium-Ion Batteries. *J. Mater. Chem. A* **2019**,7 (8), 3874-3881.

(36) Dai, F.; Yi, R.; Yang, H.; Zhao, Y.; Luo, L.; Gordin, M. L.; Sohn, H.; Chen, S.; Wang, C.; Zhang, S. Minimized Volume Expansion in Hierarchical Porous Silicon Upon Lithiation. *ACS Appl. Mater. Interfaces* **2019**,11 (14), 13257-13263.

(37) Jia, H.; Li, X.; Song, J.; Zhang, X.; Luo, L.; He, Y.; Li, B.; Cai, Y.; Hu, S.; Xiao, X.; Wang, C.; Rosso, K. M.; Yi, R.; Patel, R.; Zhang, J.-G. Hierarchical Porous Silicon Structures with Extraordinary Mechanical Strength as High-Performance Lithium-Ion Battery Anodes. *Nat. Commun.* **2020**,11 (1).

(38) Zuo, X. X.; Xia, Y. G.; Ji, Q.; Gao, X.; Yin, S. S.; Wang, M. M.; Wang, X. Y.; Qiu, B.; Wei, A. X.; Sun, Z. C.; Liu, Z. P.; Zhu, J.; Cheng, Y.-J. Self-Templating Construction of 3d Hierarchical Macro-/Mesoporous Silicon from 0d Silica Nanoparticles. *ACS Nano* **2016**,11 (1), 889-899.

(39) Zuo, X. X.; Wang, X. Y.; Xia, Y. G.; Yin, S. S.; Ji, Q.; Yang, Z. H.; Wang, M. M.; Zheng, X. F.; Qiu, B.; Liu, Z. P.; Zhu, J.; Muller-Buschbaum, P.; Cheng, Y. J. Silicon/Carbon Lithium-Ion Battery Anode with 3d Hierarchical Macro-/Mesoporous Silicon Network: Self-Templating Synthesis Via Magnesiothermic Reduction of Silica/Carbon Composite. *J. Power Sources* **2019**,412, 93-104.

(40) Li, K. Y.; Xie, H.; Liu, J.; Ma, Z. S.; Zhou, Y. C.; Xue, D. F. From Chemistry to Mechanics: Bulk Modulus Evolution of Li-Si and Li-Sn Alloys Via the Metallic Electronegativity Scale. *Phys. Chem. Chem. Phys.* **2013**,15 (40), 17658-17663.

(41) Zhao, K. J.; Wang, W. L.; Gregoire, J.; Pharr, M.; Suo, Z. G.; Vlassak, J. J.; Kaxiras, E. Lithium-Assisted Plastic Deformation of Silicon Electrodes in Lithium-Ion Batteries: A First-Principles Theoretical Study. *Nano Lett.* **2011**,11 (7), 2962-2967.

(42) Fan, F. F.; Huang, S.; Yang, H.; Raju, M.; Datta, D.; Shenoy, V. B.; van Duin, A. C. T.; Zhang, S. L.; Zhu, T. Mechanical Properties of Amorphous LixSi Alloys: A Reactive Force Field Study. *Model. Simul. Mater. Sci. Eng.* **2013**,21 (7), 074002.

(43) Huang, S.; Fan, F.; Li, J.; Zhang, S.; Zhu, T. Stress Generation During Lithiation of High-Capacity Electrode Particles in Lithium Ion Batteries. *Acta Mater.* **2013**,61 (12), 4354-4364.

(44) Chew, H. B.; Hou, B.; Wang, X.; Xia, S. Cracking Mechanisms in Lithiated Silicon Thin Film Electrodes. *IJSS* **2014**,51 (23), 4176-4187.

(45) Ge, M.; Rong, J.; Fang, X.; Zhou, C. Porous Doped Silicon Nanowires for Lithium Ion Battery Anode with Long Cycle Life. *Nano Lett.* **2012**,12 (5), 2318-2323.

- (46) Li, X.; Gu, M.; Hu, S.; Kennard, R.; Yan, P.; Chen, X.; Wang, C.; Sailor, M. J.; Zhang, J.-G.; Liu, J. Mesoporous Silicon Sponge as an Anti-Pulverization Structure for High-Performance Lithium-Ion Battery Anodes. *Nature Communications* **2014**, *5*, 4105.
- (47) Yao, Y.; McDowell, M. T.; Ryu, I.; Wu, H.; Liu, N.; Hu, L.; Nix, W. D.; Cui, Y. Interconnected Silicon Hollow Nanospheres for Lithium-Ion Battery Anodes with Long Cycle Life. *Nano Lett.* **2011**, *11* (7), 2949-2954.
- (48) Shi, L.; Wang, W.; Wang, A.; Yuan, K.; Yang, Y. Understanding the Impact Mechanism of the Thermal Effect on the Porous Silicon Anode Material Preparation Via Magnesiothermic Reduction. *J. Alloys Compd.* **2016**, *661*, 27-37.
- (49) An, Y.; Fei, H.; Zeng, G.; Ci, L.; Xiong, S.; Feng, J.; Qian, Y. Green, Scalable, and Controllable Fabrication of Nanoporous Silicon from Commercial Alloy Precursors for High-Energy Lithium-Ion Batteries. *Acs Nano* **2018**, *12* (5), 4993-5002.
- (50) Zhang, L.; Deng, J.; Liu, L.; Si, W.; Oswald, S.; Xi, L.; Kundu, M.; Ma, G.; Gemming, T.; Baunack, S.; Ding, F.; Yan, C.; Schmidt, O. G. Hierarchically Designed Sio<sub>x</sub>/Sio<sub>y</sub> Bilayer Nanomembranes as Stable Anodes for Lithium Ion Batteries. *Adv. Mater.* **2014**, *26* (26), 4527-32.
- (51) Ju, Y.; Tang, J. A.; Zhu, K.; Meng, Y.; Wang, C.; Chen, G.; Wei, Y.; Gao, Y. Sio X /C Composite from Rice Husks as an Anode Material for Lithium-Ion Batteries. *Electrochim. Acta* **2016**, *191*, 411-416.
- (52) Zhang, J.; Zhang, C.; Liu, Z.; Zheng, J.; Zuo, Y.; Xue, C.; Li, C.; Cheng, B. High-Performance Ball-Milled Sio<sub>x</sub> Anodes for Lithium Ion Batteries. *J. Power Sources* **2017**, *339*, 86-92.
- (53) Sun, L. M.; Wang, X. H.; Susantyoko, R. A.; Zhang, Q. Copper-Silicon Core-Shell Nanotube Arrays for Free-Standing Lithium Ion Battery Anodes. *J. Mater. Chem. A* **2014**, *2* (37), 15294-15297.
- (54) Na, R.; Liu, Y.; Wu, Z.-P.; Cheng, X.; Shan, Z.; Zhong, C.-J.; Tian, J. Nano-Silicon Composite Materials with N-Doped Graphene of Controllable and Optimal Pyridinic-to-Pyrrolic Structural Ratios for Lithium Ion Battery. *Electrochim. Acta* **2019**, *321*.
- (55) Kim, B.; Ahn, J.; Oh, Y.; Tan, J.; Lee, D.; Lee, J.-K.; Moon, J. Highly Porous Carbon-Coated Silicon Nanoparticles with Canyon-Like Surfaces as a High-Performance Anode Material for Li-Ion Batteries. *J. Mater. Chem. A* **2018**, *6* (7), 3028-3037.
- (56) Zhang, Y.-C.; You, Y.; Xin, S.; Yin, Y.-X.; Zhang, J.; Wang, P.; Zheng, X.-s.; Cao, F.-F.; Guo, Y.-G. Rice Husk-Derived Hierarchical Silicon/Nitrogen-Doped Carbon/Carbon Nanotube Spheres as Low-Cost and High-Capacity Anodes for Lithium-Ion Batteries. *Nano Energy* **2016**, *25*, 120-127.
- (57) Sun, W.; Hu, R.; Zhang, M.; Liu, J.; Zhu, M. Binding of Carbon Coated Nano-Silicon in Graphene Sheets by Wet Ball-Milling and Pyrolysis as High Performance Anodes for Lithium-Ion Batteries. *J. Power Sources* **2016**, *318*, 113-120.
- (58) Zhou, Z.-W.; Liu, Y.-T.; Xie, X.-M.; Ye, X.-Y. Constructing Novel Si@Sno<sub>2</sub> Core-Shell Heterostructures by Facile Self-Assembly of Sno<sub>2</sub> Nanowires on Silicon Hollow Nanospheres for Large, Reversible Lithium

Storage. *ACS Appl. Mater. Interfaces* **2016**, *8* (11), 7092-7100.

(59) Bok, T.; Choi, S.; Lee, J.; Park, S. Effective Strategies for Improving the Electrochemical Properties of Highly Porous Si Foam Anodes in Lithium-Ion Batteries. *J. Mater. Chem. A* **2014**, *2* (34), 14195-14200. (60)

Sohn, M.; Kim, D. S.; Park, H.-I.; Kim, J.-H.; Kim, H. Porous Silicon-Carbon Composite Materials Engineered by Simultaneous Alkaline Etching for High-Capacity Lithium Storage Anodes. *Electrochim. Acta* **2016**, *196*, 197-205.

(61) Li, X.; Gu, M.; Hu, S.; Kennard, R.; Yan, P.; Chen, X.; Wang, C.; Sailor, M. J.; Zhang, J.-G.; Liu, J. Mesoporous Silicon Sponge as an Anti-Pulverization Structure for High-Performance Lithium-Ion Battery Anodes. *Nat. Commun.* **2014**, *5*.

(62) Zhao, K.; Pharr, M.; Vlassak, J. J.; Suo, Z. Inelastic Hosts as Electrodes for High-Capacity Lithium-Ion Batteries. *J. Appl. Phys.* **2011**, *109*, 016110.

(63) Huang, S.; Fan, F.; Li, J.; Zhang, S.; Zhu, T. Stress Generation During Lithiation of High-Capacity Electrode Particles in Lithium Ion Batteries. *Acta Mater.* **2013**, *61*, 4354–4364.

(64) Chew, H. B.; Hou, B. Y.; Wang, X. J.; Xia, S. M. Cracking Mechanisms in Lithiated Silicon Thin Film Electrodes. *Int. J. Solids Struct.* **2014**, *51* (23-24), 4176-4187.

## TABLE of CONTENT

Macro-/mesoporous silicon with tunable pore size and wall thickness was successfully synthesized by varying the magnesiothermic reduction time in the range of from 4 hours to 8 hours and 16 hours, where the porous silicon with small wall thickness and large pore size exhibits better capacity retention, as revealed by both experimental performance results and finite element analysis.

